International Journal of Coal Science & Technology (2026) 13:6
https://doi.org/10.1007/s40789-025-00840-y

RESEARCH

Damage characteristic of split-re-closed shale under impact shearing

Wei Tang[1] · Cheng Zhai[1] · Ting Liu[1] · Jizhao Xu[1] · Yong Sun[1] · Yangfeng Zheng[1] · Yuzhou Cong[1] · Yu Wang[1] · Chengjian Pi[2]

Received: 4 February 2025 / Revised: 5 August 2025 / Accepted: 7 November 2025

Abstract
This study proposes methane in-situ explosive fracturing (MIEF) for reactivating closed fractures in aging shale gas reservoirs. Employing a split Hopkinson pressure bar (SHPB) system, this study investigates the impact-shearing damage characteristics of the split-re-closed shales. Changes in fracture surface roughness are analyzed via 3D laser scanning, and fracture spaces are reconstructed and quantified using X-ray tomography. Based on numerical simulation methods, the impact-shearing damage process of reclosed fractures is discussed. Results show that rock debris exfoliation during impact shearing reduces fracture surface roughness, with roughness parameters Z_{2s} and $\theta_{max}/(C+1)$ exhibiting a linear positive correlation. The 3D box dimension of fracture surfaces decreases after impact shearing and shows an exponential correlation with parameter Z_{2s}. The 2D box dimension of the damaged areas of the fracture surface displays fractal characteristics and exponential positive correlations with both Z_{2s} and $\theta_{max}/(C+1)$. Fracture apertures in split-re-closed shale samples increase by 5–19 times after impact shearing, with the increment positively correlating with roughness parameter Z_{2s}. Areas with high roughness initiate damage earliest during impact shearing, and periodic "shear dilation – fracture damage" cycles between the upper and lower fracture surfaces lead to (1) non-uniform damage distribution, (2) rock debris exfoliation, and (3) shear misalignment. These effects collectively prevent complete fracture closure, thereby generating self-propping behavior in impact-sheared fractures.

Keywords Split-re-closed shale · Impact shearing · Fracture surface roughness · Fracture space distribution · Fracture damage

1 Introduction

The shale gas revolution has dramatically reshaped the global energy landscape. However, as the number of shale gas wells increases, the issue of low production from aging wells is gaining increasing attention (Gu et al. 2022; Shi et al. 2022). Production data from 640 wells in the Haynesville area of the United States reveals that newly drilled wells exhibit an average production decline of 72% in the first year, climbing to 86% by the end of the second year (Guo et al. 2016a, b). Furthermore, the three-year production decline rates for shale gas in regions such as Woodford, Eagleford, Barnett, and Fayetteville range from 77% to 89% (Asala et al. 2016; Guo et al. 2016a, b). This rapid productivity decline underscores the persistent challenge of underperformance in shale gas wells (Patzek et al. 2013; Saputra et al. 2021).

To date, the primary re-stimulation technology for aging wells remains hydraulic fracturing— also termed re-fracturing or second fracturing (Lei et al. 2019; Wang et al. 2021; Yi et al. 2022). Over the past 53 years, re-fracturing has been applied in Pembina oil field in Canada, where 77% of projects achieved satisfactory results (Vincent 2011). These applications confirm that aging wells re-stimulation can enhance their production. However, re-fracturing still presents environmental pollution risks. Compared to the first fracturing, re-fracturing consumes more water, and its construction process is more complex (French et al. 2014;

✉ Cheng Zhai
greatzc@cumt.edu.cn

[1] School of Safety Engineering, China University of Mining and Technology, Xuzhou 221116, China

[2] Baodian Coal Mine, Yankuang Energy Group Company Limited, Zoucheng 273500, China

Published online: 28 January 2026

Kong et al. 2019; Vincent 2010). Moreover, re-fracturing technology is still a static fracturing method with a limited number of fractures, making it difficult to form a complex fracture network in shale reservoirs (Chen et al. 2022; Lv et al. 2024).

Given that aging shale gas wells still maintain some level of production despite their low production rates, this study proposes a novel conceptual method—methane in-situ explosion fracturing (MIEF)—for aging wells re-stimulation. As illustrated in Fig. 1, MIEF utilizes in-situ desorbed shale gas (IDSG, primarily methane) as the energy medium for reservoir fracturing. By artificially injecting combustion-supporting agents (CSAs) into underground wells and detonating the gas mixture, the shockwaves generated by methane in-situ explosion can fracture the shale reservoir and re-activate the seepage capacity of the stress-closed hydraulic fractures, to establish complex seepage networks and ultimately boost old wells' production. Unlike hydraulic fracturing, methane explosion is a dynamic impact process. Therefore, exploring the mechanical behavior of shale under dynamic impact loading will provide critical insights into optimizing MIEF technology.

The split Hopkinson pressure bar (SHPB) system is currently the most widely adopted technique for determining the dynamic mechanical properties of materials (Xie et al. 2020; Yang et al. 2020). In recent studies, Liu et al. (2015) proposed and established a dynamic constitutive model of shale under uniaxial impact loads, based on statistical damage theory and experimental results of shale deformation and damage characteristics under impact loading. Shi et al. (2019) prepared notched semi-circular bend (NSCB) samples and integrated the finite element method with J-integral to obtain the dynamic fracture toughness. Yang et al. (2019) also used the NSCB samples to investigate the fracture pattern under impact loading. Fan et al. (2021) used the SHPB system equipped with thermos-mechanical coupling equipment to study the dynamic stress–strain curve, peak stress, peak strain, elastic modulus, and energy partition. Wang et al. (2022) prepared single-cleavage triangular (SCT) shale samples for impact experiments and employed the AUTODYN program to simulate the dynamic fracture behavior of the cracks. Luo et al. (2022) further explored shale failure modes under different confining pressures and bedding directions. Liu et al. (2023) used the SHPB system to conduct dynamic-static combined impact experiments on circular-hole-containing shale samples with different bedding angles, and recorded the damage process using digital image correlation (DIC) technology. Feng et al. (2023) used the SHPB and DIC technologies to perform impact Brazilian split tests, and discussed the deformability and tensile strength of shales.

Current research mainly focuses on the dynamic mechanical properties of shale. However, re-closed fractures are present in shale reservoirs of aging wells, and there have been no reports on the damage of split-re-closed shale under impact shearing. In this study, shale samples were first split and subsequently re-closed for impact-shearing tests. By employing the SHPB system, a three-dimensional laser scanner, an X-ray micro-imaging system, and conducting numerical simulations, we explored changes in fracture surface roughness, the evolution of fracture space, as well as the damage characteristics and processes of split-re-closed shale under impact shearing.

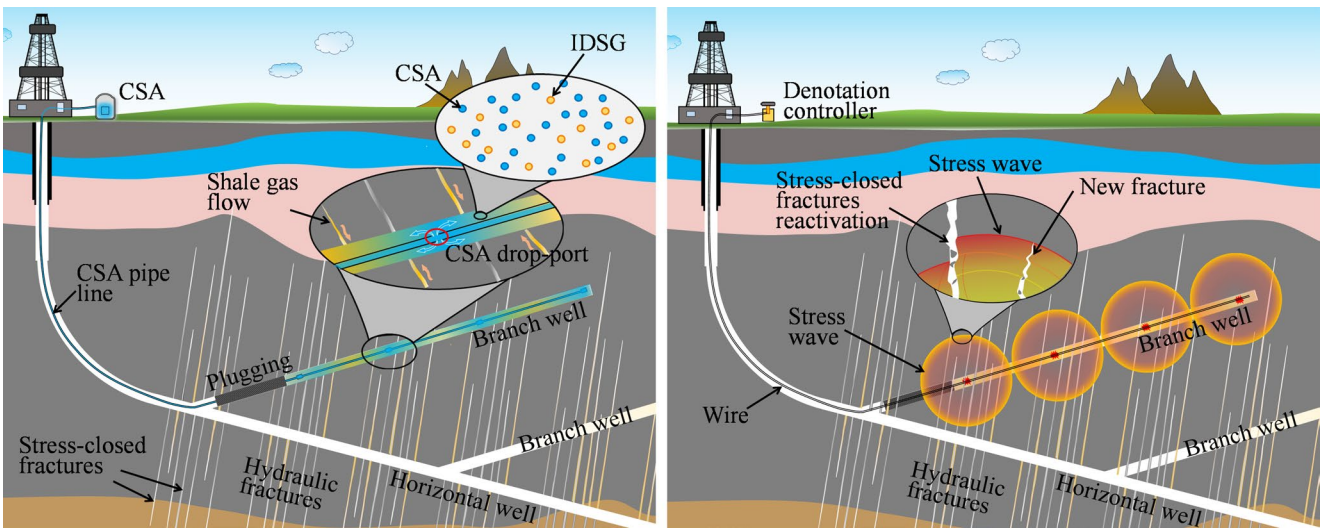

Fig. 1 Schematic diagram of methane in-situ explosion fracturing

2 Experiment of split-re-close shale sample

2.1 Sample preparation

The Sichuan Basin is a key shale gas development area in China, and the shale samples used in the experiments were collected from shale outcrops in the Changning area of Sichuan, China. The mineral composition of the shale samples was characterized using a D8 Advance X-ray diffractometer (Bruker Corporation, Germany). Results showed that the primary components are quartz (56.7%), calcite (25.1%) and dolomite (9.5%).

The shale was machined into cylindrical samples with a diameter of 50 mm and a height of 50 mm, and a 3 mm-deep groove was cut on one end face. To prepare the split-re-closed samples, the intact shale samples were first split using an electro-hydraulic servo universal testing machine. The groove orientation was aligned with the loading direction to maximize the likelihood of inducing a central splitting fracture. As shown in Fig. 2, red dye was used to stain the split surfaces to facilitate observation of post-impact shear changes. This dyeing process is physically-based and does not significantly alter the split surfaces' properties. A total of 22 samples were prepared for the experimental program.

2.2 Tests on methane explosion pressure

To measure the explosive pressure of methane-oxygen mixtures under high-pressure conditions, a high-pressure methane explosive tube (as shown in Fig. 3a) was constructed. The tube was made of Q235 steel, with dimensions of 1000 mm in length, 100 mm in inner diameter, and 50 mm in wall thickness, and it has a pressure resistance of 150 MPa. Both ends of the tube were flanged to form a sealed chamber. The end with the gas inlet was connected via piping to high-purity methane and oxygen cylinders, which supplied gas to the explosion tube. The tube was equipped with a pressure gauge and a high-energy electric spark plug for ignition. A total of three dynamic pressure sensors are mounted on the tube, positioned 0.5 m, 0.6 m, and 0.7 m from the ignition end, respectively. These pressure sensors, in conjunction with a dynamic overpressure acquisition instrument, were used to measure the explosion pressure during experiments. The signal acquisition instrument was the TST6300 dynamic data acquisition system, manufactured by Chengdu TST Electronic Information Co., Ltd. The pressures of methane and oxygen in the tube were configured at a ratio of 1:2. A total of two test schemes were designed, with total initial pressures (p_0) set to 1.8 MPa and 2.4 MPa respectively. Figure 3b showed that when the initial pressure of the methane-oxygen mixtures in the tube were 1.8 MPa and 2.4 MPa, the maximum explosion pressures reached 72.4 MPa and 89.7 MPa, respectively. By fitting the linear rising segments of the explosion pressure curves, the pressure rise rates (v) under the initial pressures of 1.8 MPa and 2.4 MPa were 343 GPa/s and 430 GPa/s, respectively.

Fig. 2 Splitting and dyeing of shale samples

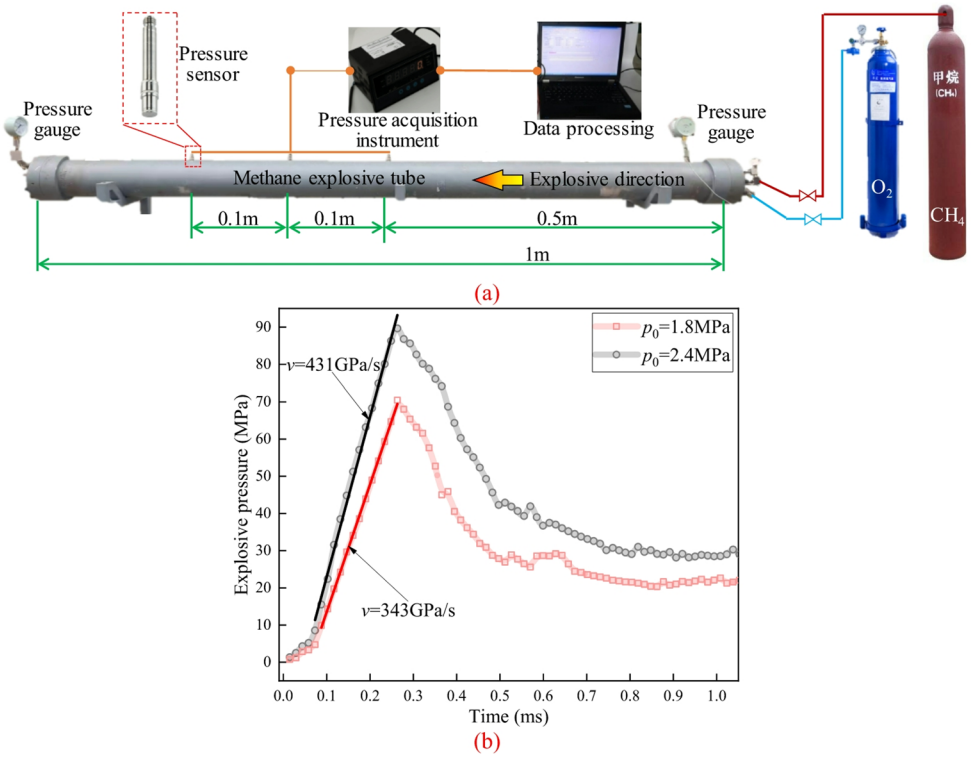

Fig. 3 **a** Experimental system for testing explosive pressures of methane-oxygen mixture; **b** Explosive pressures of methane-oxygen mixtures

2.3 Experimental system and dynamic splitting strength of shale

Figure 4a shows the improved SHPB experimental system, manufactured by Luoyang Weili Technology Co., Ltd., China. Both the incident bar and the transmitted bar are made of high-strength alloy steel, each measuring 3000 mm in length. The elastic modulus, density, and Poisson's ratio of the alloy steel are 210 GPa, 7900 kg/m^3, and 0.27 respectively. The air pressure in the air chamber can be adjusted in 0.1-MPa increments, with air release controlled by a solenoid valve. The released high-pressure gas propels the bullet against the incident bar and generates a stress wave. Split-re-closed samples are held in place during the experiment by a gripper, which can apply confining pressure to the sample via an oil pump.

Before conducting the impact shear experiments on split-re-closed shale samples, the dynamic splitting strengths of shales were measured using the SHPB system under impact air pressures of 0.2 MPa and 0.3 MPa. The dynamic stress equilibrium curves during the experiments were shown in Figs. 4b and c. At the air pressures of 0.2 MPa and 0.3 MPa, the maximum stresses generated by the bullet in the incident bar reached 72.4 MPa and 80.6 MPa, respectively. Linear fitting yielded the pressure rise rates (v) of 305 GPa/s and 452 GPa/s, which closely matched the methane explosion pressure rise rates. Additionally, the corresponding dynamic splitting strengths of shales under the two pressure rise rates were 17.2 MPa and 18.8 MPa.

2.4 Experimental scheme

The research workflow is illustrated in Fig. 5. Prior to the impact-shearing experiments, the fracture surfaces of split samples were first scanned using a three-dimensional laser scanner to obtain initial fracture surface height data. The laser scanner was the KEYENCE VR5000 Series, featuring a maximum measurement range of 200 × 100 × 50 mm³ and a resolution of 0.1 μm. The corresponding software was used to generate surface height profiles and geometric models from the scanned data. After scanning, samples were manually re-closed, and two shims were affixed to the ends of each re-closed sample. The shims, fabricated from alloy steel, had a thickness of 5 mm and a size slightly smaller than the end faces of the re-closed samples to avoid interfering with shear behaviors during impact. The shims were bonded to the samples' end faces using vacuum silicone grease, following which impact-shearing experiments were conducted as depicted in Fig. 4a. The lower portion of the sample in the clamp served as the fixed side (in contact with the transmitted bar), while the upper portion (in contact with the incident bar) acted as the impact side. Vacuum silicone grease was applied to the interfaces between the bars and the sample. No axial pre-stress was applied to the bars to prevent initial stress from damaging the fracture surface.

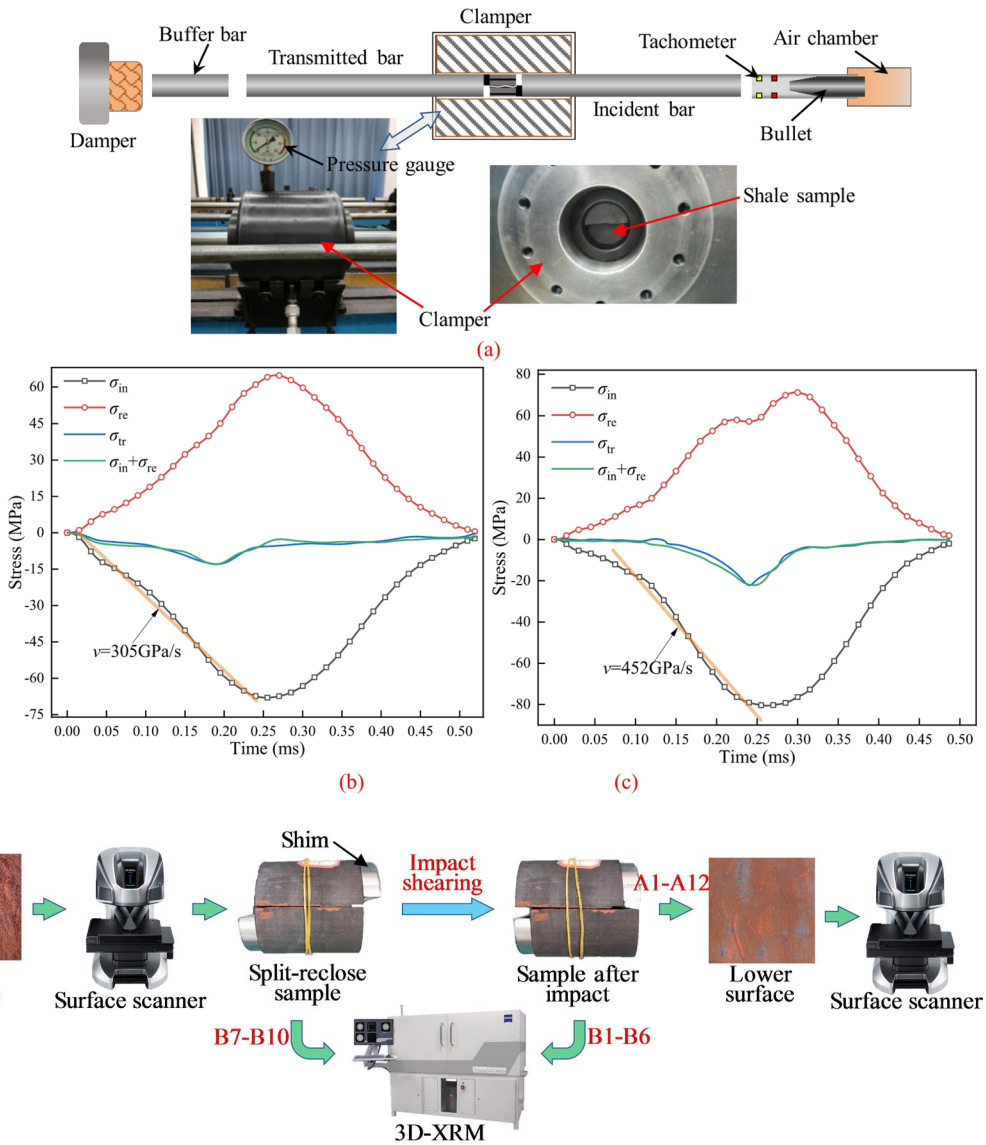

Fig. 4 **a** Experimental system for impact-induced shearing; **b** and **c** Dynamic stress equilibrium during dynamic Brazilian splitting tests of shales under the air pressures of 0.2 MPa and 0.3 MPa

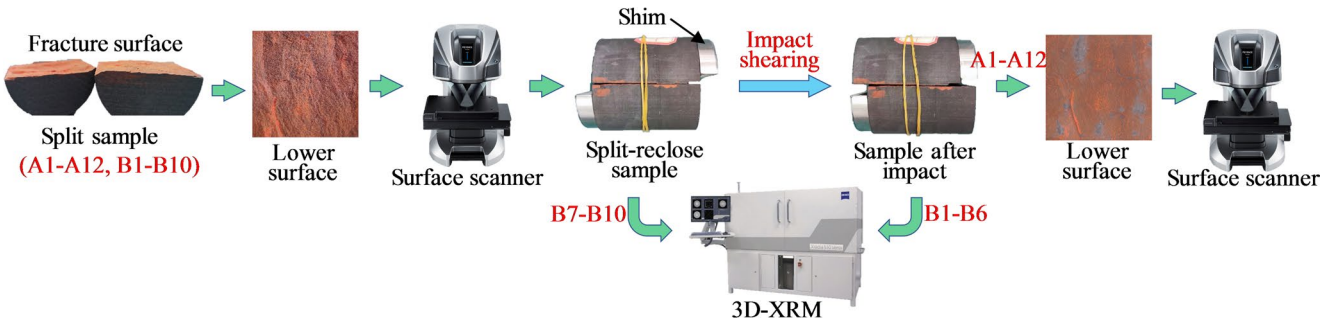

Fig. 5 Laser scanning of fracture surface

To investigate the mechanical behavior of split-re-closed samples under different confining pressures, 22 samples were divided into two groups: Group A (A1–A12) was subjected to a confining pressure of 1 MPa, while Group B (B1–B10, with B1–B6 as the experimental subgroup and B7–B10 as the control subgroup) was subjected to a confining pressure of 5 MPa. Air pressures for propelling the bullet were set to 0.2 MPa and 0.3 MPa for Groups A and B, respectively. The upper portions of the samples, driven by the stress wave, underwent a maximum shear displacement equal to one shim thickness to complete the impact-shearing process. After testing Group A samples, the rock debris generated during the impact process was removed, and the fracture surfaces were rescanned to obtain post-test height data. In this study, the lower fracture surfaces of all samples were scanned. For Group B, samples B1–B6 were wrapped in heat-shrink films to preserve the fracture space geometry as intact as possible after the experiments, while samples B7–B10 were not subjected to impact-shearing tests. All Group B samples were subsequently scanned using a three-dimensional X-ray micro-imaging (3D-XRM) system, specifically the Xradia 510 Versa (Carl Zeiss).

3 Results and analysis

3.1 Changes in fracture surface roughness

Three-dimensional laser scanning results of fracture surfaces (Group A) before impact shearing are shown in Fig. 6a, with

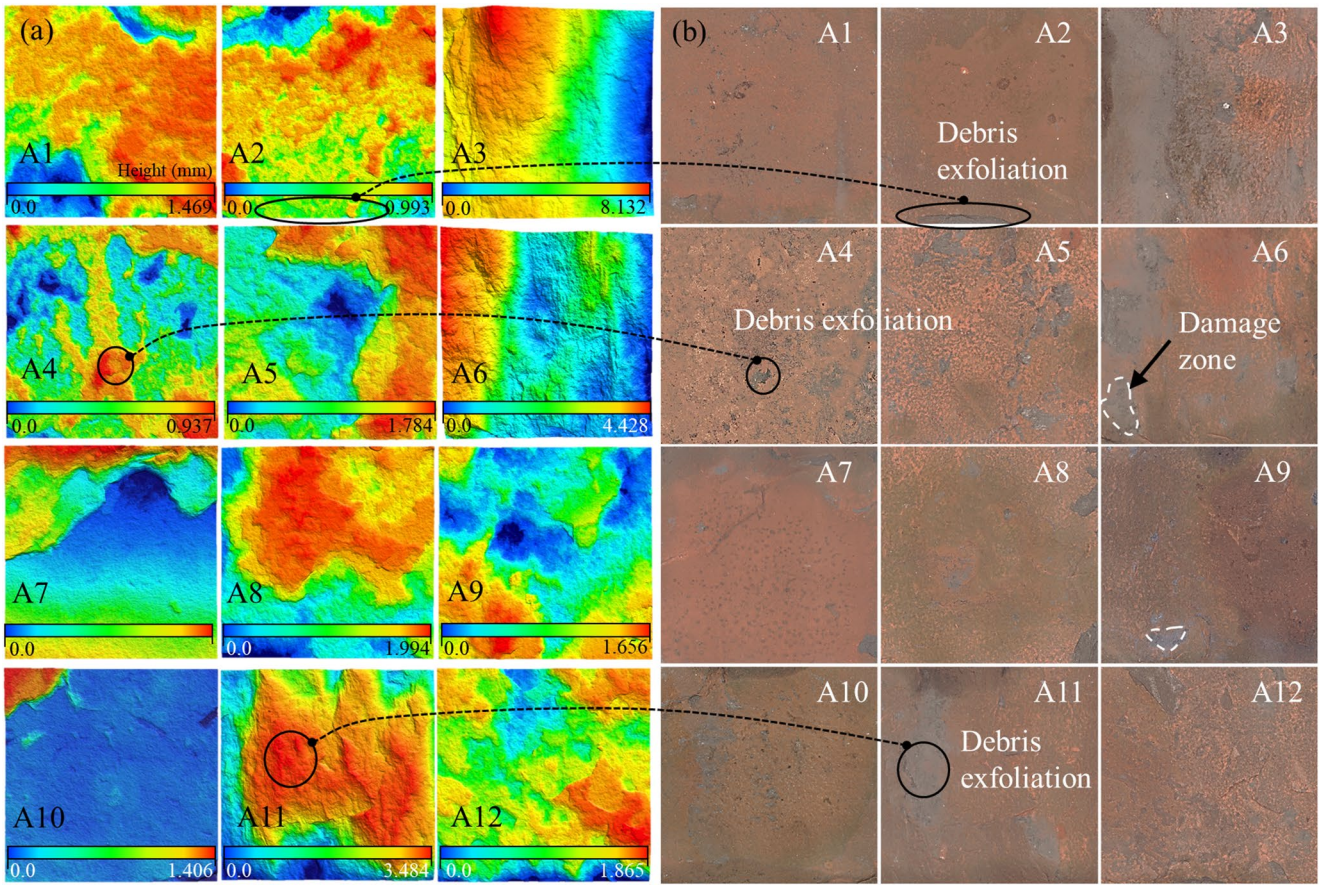

Fig. 6 **a** Fracture surface heights (before impact shearing) and **b** Fracture damage distributions (after impact shearing)

the scale bar in millimeters. The concept of fracture surface roughness (FSR) was introduced by Barton (1973), and the maximum roughness height, defined as the maximum height of the fracture surfaces, is one of the parameters to characterize the FSR. As shown in the figure, the maximum height of sample A3 exceeded 8 mm, while those of samples A6 and A11 both exceeded 3 mm, indicating that these three samples had higher FSR. In contrast, the maximum roughness heights of samples A2 and A4 were both less than 1 mm, reflecting relatively low FSR. Figure 6b shows the morphologies of the fracture surfaces after impact shearing, with the gray areas representing the damage zones. All samples exhibited debris exfoliation on their fracture surfaces, and samples A3, A6, and A11 displayed larger damage zones. Within the black-circled damage zones, severe debris exfoliation was primarily distributed in regions with higher surface elevations.

The maximum roughness height is defined by only two points, and fails to characterize the detailed features of the fracture surface. The root-mean-square value of the first derivative of height (Z_{2s}) is another parameter used to quantify FSR, which can describe the undulating properties of the entire surfaces. A larger Z_{2s} value means a rougher fracture surface. The definition of Z_{2s} is presented in Eq. (1), with Eq. (2) representing the discretized form for surface point clouds (Huan et al. 2024; Vogler et al. 2017). l_x and l_y are the surface lengths in the X and Y directions; n and m are the numbers of discretization points along the X and Y axes; and Δx and Δy represent the point spacings in the X and Y directions.

$$Z_{2s} = \left(\frac{1}{l_x l_y}\int_0^{l_x}\int_0^{l_y}\left(\left(\frac{\partial z(x,y)}{\partial x}\right)^2 + \left(\frac{\partial z(x,y)}{\partial y}\right)^2\right)\mathrm{d}x\mathrm{d}y\right)^{\frac{1}{2}} \tag{1}$$

$$Z_{2s} = \frac{1}{(n-1)(m-1)}\left[\sum_{j=1}^{m-1}\sum_{i=1}^{n-1}\frac{(z_{i+1,j}-z_{i,j})^2+(z_{i+1,j+1}-z_{i,j+1})^2}{2\Delta x^2} + \sum_{j=1}^{m-1}\sum_{i=1}^{n-1}\frac{(z_{i,j+1}-z_{i,j})^2+(z_{i+1,j+1}-z_{i+1,j})^2}{2\Delta y^2}\right]^{\frac{1}{2}} \tag{2}$$

The Z_{2s} values of the 12 fracture surfaces before and after impact shearing are shown in Fig. 7a. The Z_{2s} values ranged from 0.191 to 0.396 before impact shearing and decreased to 0.184–0.387 after testing; 7 of the 12 samples exhibited reduced Z_{2s} values, indicating that the FSR tended to decrease

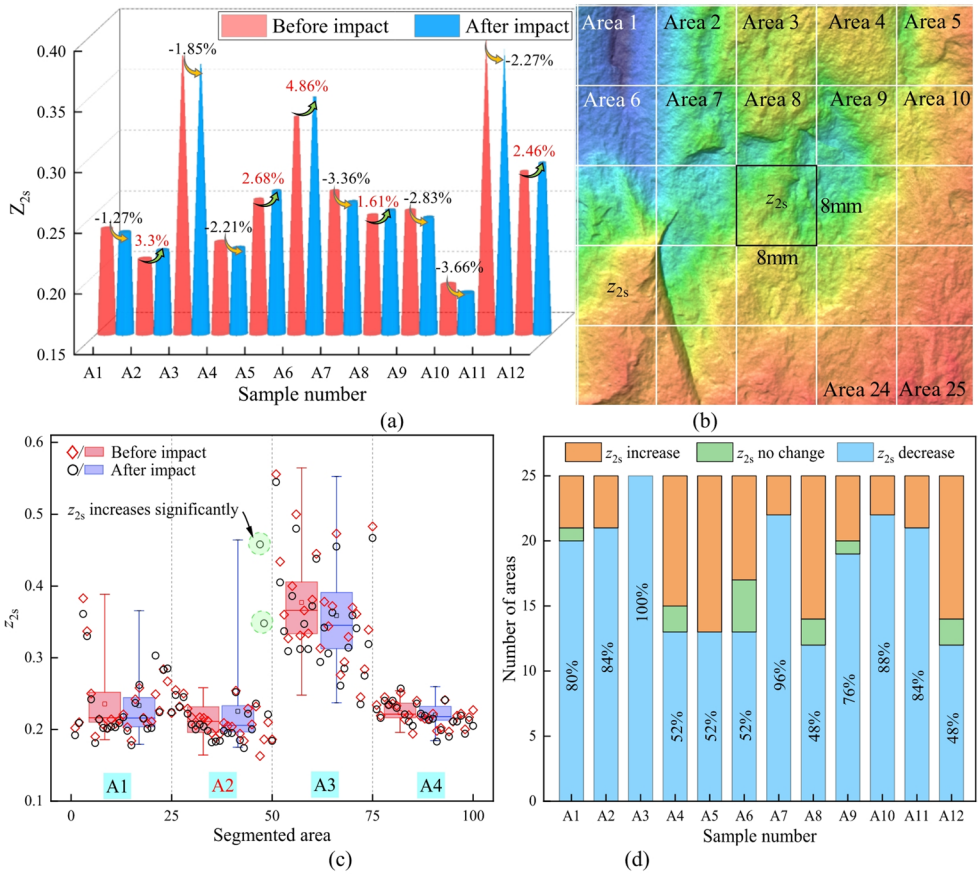

Fig. 7 Statistics of the root-mean-square values of first derivative of height. **a** Changes in Z_{2s} of fracture surfaces; **b** Fracture surface segmentation; **c** z_{2s} statistics of samples A1–A4; **d** Changes in z_{2s} of samples

after impact shearing. Given that Fig. 6b reveals uneven distributions of damage zones on the fracture surfaces, each fracture surface was further divided into 25 subregions, as shown in Fig. 7b. To distinguish these localized measurements, the root-mean-square values of the first derivative of height for each subregion is denoted as z_{2s}. Figure 7c shows the z_{2s} results, using samples B1–B4 as examples. Red and black dots represent the z_{2s} values before and after impact shearing, respectively. The box-plots reflect the maximum, minimum, average, and median z_{2s} values across the 25 subregions of each fracture surface; the upper and lower box boundaries cover 25%–75% of the data ranges. Box heights indicate the degree of data dispersion, while the box lengths reflect the uniformity of z_{2s} distributions.

Observing the data points within the green circle in the figure, sample A2 showed a significant increase in z_{2s} in two subregions after impact. Additionally, box length remained almost unchanged, indicating that the z_{2s} variations of most subregions were insignificant. However, as shown in Fig. 7a, the overall Z_{2s} of sample A2 increased by 3.3% after impact shearing, demonstrating that local FSR elevations contributed to increased overall surface roughness. Moreover, the median z_{2s} value of sample A2 decreased after impact shearing, indicating that most of the z_{2s} decreased. The longer box plot for sample A3 meant a more dispersed distribution of z_{2s}, corresponding to higher fracture roughness. In contrast, the shorter box length for sample A4 reflected lower FSR. The median value of z_{2s} for all four samples decreased, consistent with the general trend of reduced FSR after impact shearing. Subregions with post-impact z_{2s} change less than 0.001 were considered unchanged. Across the 300 subregions of the 12 fracture surfaces, 25% of subregions exhibited increased z_{2s} while 71% showed decreases, confirming that impact shearing primarily reduces fracture surface roughness.

The FSR exhibits intrinsic directional anisotropy. Grasselli and Egger (2003) proposed the parameter $\theta_{max}/(C+1)$ to describe the FSR variations across different directions, supported by rigorous theoretical validation. This parameter quantifies the average inclination of the fracture surface, while θ_{max} is the maximum inclination angle in the selected direction, and C is a roughness parameter intrinsic to the fracture surface. The $\theta_{max}/(C+1)$ values across different directions before and after impact shearing were calculated using the Surface Roughness Calculator-V3.0, a software developed by Magsipoc et al. (2020). Figure 8a showed the values of $\theta_{max}/(C+1)$ in different directions for samples A1–A3. The curves of samples A1 and A2 were approximately circular, indicating that the fracture surfaces were relatively smooth. In contrast, the fracture surface of sample

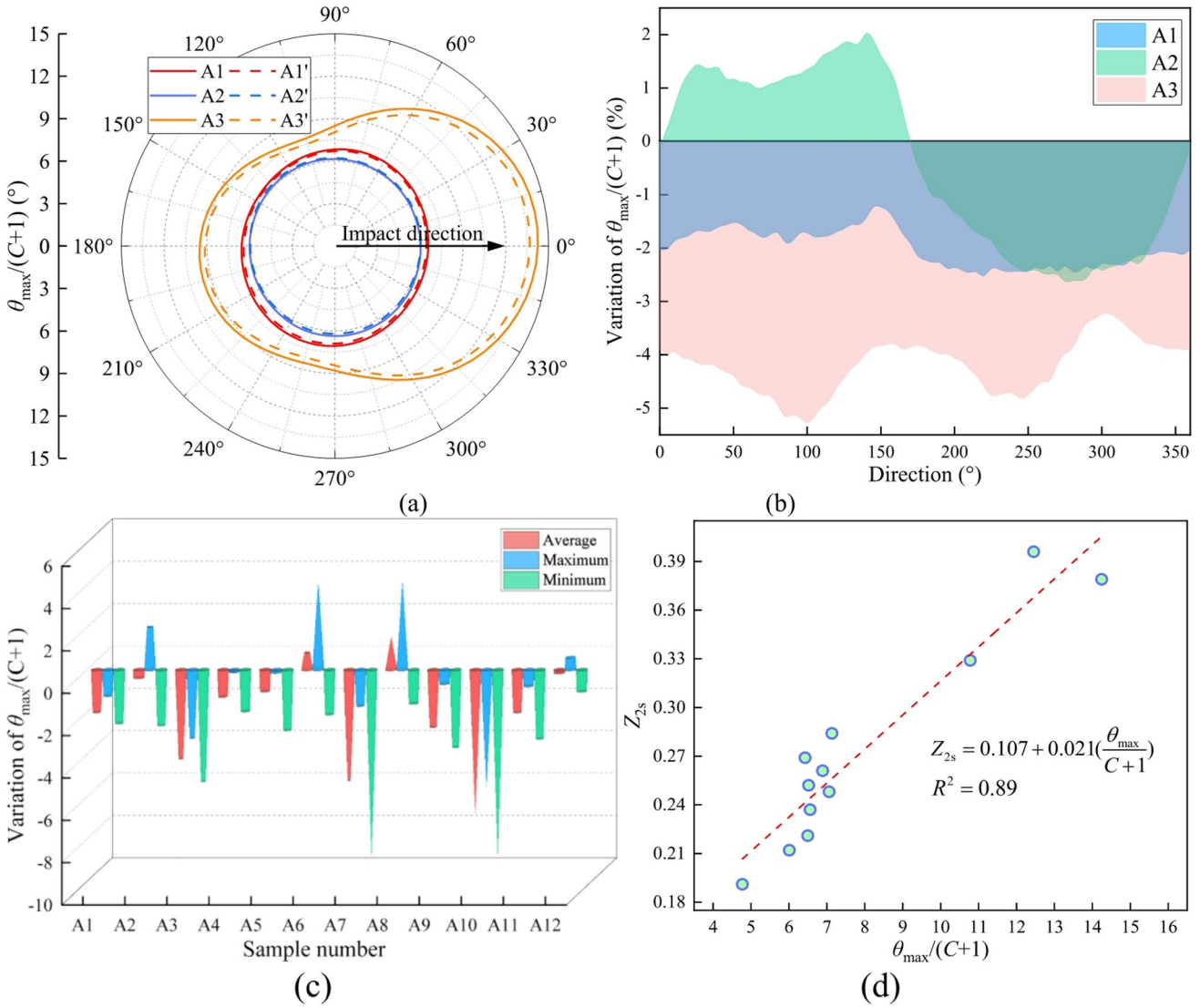

Fig. 8 Results of fracture surface $\theta_{max}/(C+1)$. **a** Statistics of θmax/(C+1) for samples A1–A3; **b** Variations of $\theta_{max}/(C+1)$ for samples A1–A3; **c** Variations of average, maximum and minimum $\theta_{max}/(C+1)$; **d** Relationship between $\theta_{max}/(C+1)$ and Z_{2s}

A3 displayed distinct anisotropy: the value of $\theta_{max}/(C+1)$ reached the maximum at 0°, corresponding to the roughest direction, which coincides with the experimental impact direction. The variations in $\theta_{max}/(C+1)$ in different directions of samples A1–A3 after impact shearing were shown in Fig. 8b. The reduction in $\theta_{max}/(C+1)$ for sample A1 is approximately 2%. For sample A3, the decrease in $\theta_{max}/(C+1)$ fluctuates, with the maximum reduction exceeding 5%. While the FSR decreases in all directions for samples A1 and A3, sample A2 shows a 1%–2% increase in $\theta_{max}/(C+1)$ over the range of 0°–170°.

Figure 8c shows the statistics of the average, maximum, and minimum values of $\theta_{max}/(C+1)$ across different directions. The changes in the average values reveal that only samples A6 and A8 exhibit increases in the $\theta_{max}/(C+1)$ values, by 0.81% and 1.57%, respectively. The maximum values of $\theta_{max}/(C+1)$ for samples A2, A6, A8, and A12 increased by 2.03%, 3.97%, 4.28%, and 0.58%, while those for all other samples decreased. In addition, the minimum $\theta_{max}/(C+1)$ values decreased for all samples. The statistics of $\theta_{max}/(C+1)$ confirm that the FSR tends to decrease after impact shearing. The parameters $\theta_{max}/(C+1)$ and Z_{2s} exhibited similar variation characteristics. Figure 8d demonstrated a linear positive correlation between the two parameters.

3.2 Fractal characteristics of damage zone on fracture surface

In addition to Z_{2s} and $\theta_{max}/(C+1)$ introduced in the preceding section, fractal dimension is another important parameter for characterizing the FSR (Yang et al. 2024). The

calculation method for the box-counting dimension of 3D fracture surface is as follows: cover the fracture surface with cubic boxes with a side length of δ; count the minimum number of boxes, $N(\delta)$, required to completely cover the fracture surface; repeat the above process for different δ values; and calculate the box-counting dimension (D) using Eq. (3) (Movassagh et al. 2021).

$$D = \lim_{\delta \to 0} \frac{\log N(\delta)}{-\log(\delta)} \tag{3}$$

For 3D fracture surfaces, fractal characteristics are indicated by D values ranging from 2 to 3; a larger D corresponds to higher surface roughness. Figure 9 illustrated the box-covering results for the fracture surface of sample A11 using different box sizes. Eleven different box sizes were selected, with the corresponding box counts for samples before and after impact shearing recorded in Tables 1 and 2, respectively. Due to the relatively small value of D for these fracture surfaces, six decimal places were retained in calculations. Results indicated that all 12 fracture surfaces exhibited fractal characteristic. The box-counting dimensions for samples A3, A6 and A11 were 2.05624, 2.05243 and 2.05727, respectively, indicating that A3, A6 and A11 had higher fracture roughness. Comparison of Tables 1 and 2 shows that D value decreased from 2.03498–2.05727 to 2.03079–2.05455, further confirming the trend of reduced FSR after impact shearing.

Figure 10a presented the statistical changes in the three-dimensional fractal dimension of the fracture surfaces for 12 samples before and after impact shearing. The D values for samples A2, A4, A6, and A9 increased after impact shearing, with the maximum increase reaching only 0.01961%. However, the D values for the other 8 samples decreased, with the minimum decrease reaching 0.03026%. Overall, these results indicate that although the D values increased for some samples, the increase rates were much smaller than the decrease rates. The D values tended to decrease after impact shearing, and the reduction of D values also corresponded to the decrease of FSR. Figure 10b presented D and Z_{2s} before impact shearing, revealing an exponential positive correlation between the D and the Z_{2s} of the fracture surface.

Figure 6b demonstrated that the fracture surface displayed distinct damage characteristics after impact shearing. Consequently, a quantitative exploration of the distribution traits of the damage zones on the fracture surface was carried out. Prior to the experiments, the fracture surfaces were pre-dyed; during impact shearing, the dye in the damaged areas was abraded, enabling damage zones to be easily extracted via color segmentation. Fracture surface images were converted to grayscales using Fiji software (Schindelin et al. 2012) and further processed into binary images, as depicted in Fig. 11. In these images, white regions represented the extracted damage zones, while black regions indicated the unaffected areas. To quantitatively characterize

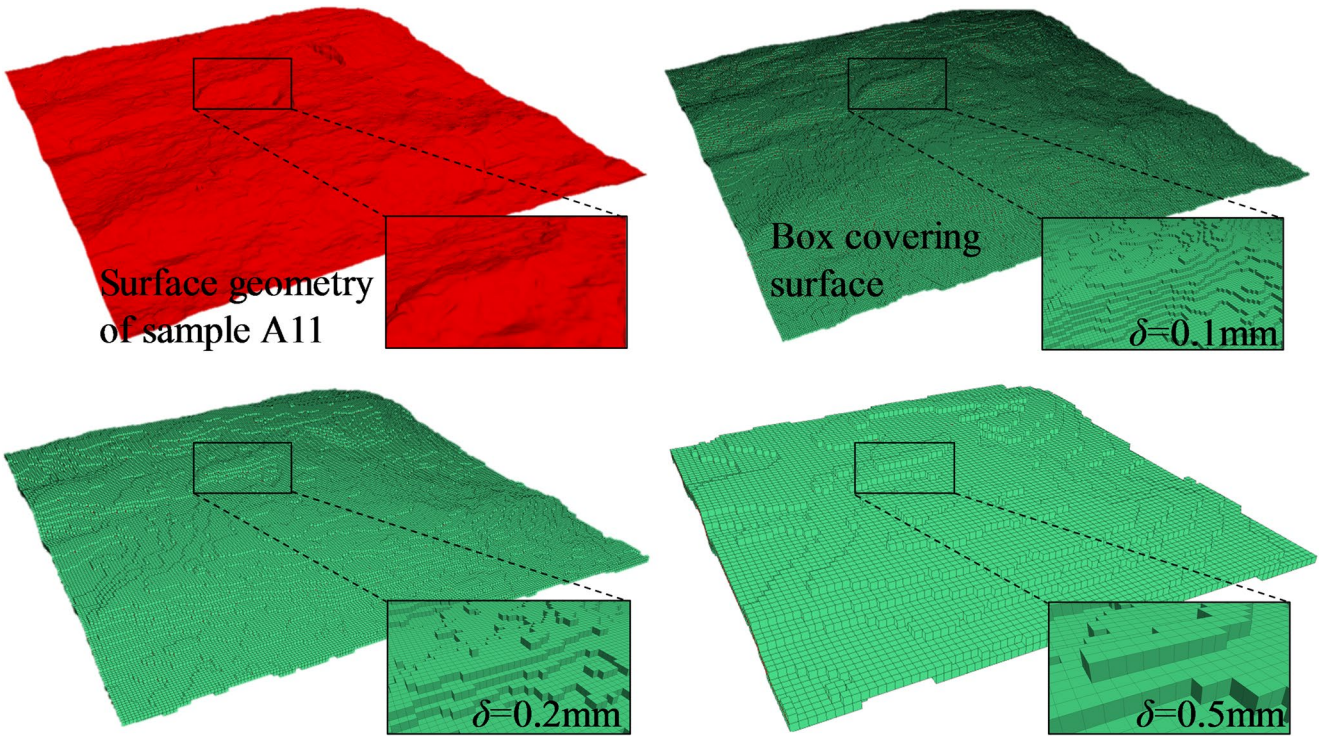

Fig. 9 Box covering for 3D fracture surface of sample A11

Table 1 Statistics of box counts before impact shearing

No.	Box size (mm) and corresponding number											D
	0.1	0.2	0.25	0.32	0.5	1.6	2	2.5	5	8	10	
A1	193,890	47,075	31,027	18,431	7854	625	400	256	100	64	25	2.04877
A2	188,363	47,177	29,633	17,448	7253	625	400	256	100	64	25	2.04006
A3	214,217	53,353	34,162	20,620	8430	764	506	298	128	75	26	2.05624
A4	189,356	46,872	29,606	18,639	7693	626	401	257	101	64	26	2.04253
A5	194,626	48,591	30,684	18,511	7622	627	400	256	100	64	25	2.05049
A6	205,959	51,158	32,835	19,794	8055	790	480	280	106	75	26	2.05243
A7	192,385	47,936	30,411	18,406	7406	651	405	256	100	64	25	2.04656
A8	192,057	47,445	30,988	18,634	7284	706	400	256	100	64	25	2.04667
A9	192,036	47,414	30,340	18,345	7517	625	400	256	100	64	25	2.04689
A10	186,666	44,335	27,057	19,767	6562	638	400	256	100	64	25	2.03498
A11	215,032	53,421	33,997	20,722	8370	743	508	323	100	92	25	2.05727
A12	196,420	48,737	31,172	18,916	7466	681	400	256	100	64	25	2.05181

Table 2 Statistics of box counts after impact shearing

No.	Box size (mm) and corresponding number											*D*
	0.1	0.2	0.25	0.32	0.5	1.6	2	2.5	5	8	10	
A1	193,446	47,035	30,942	18,358	7844	625	400	256	100	64	25	2.04815
A2	189,431	46,828	30,014	17,677	7767	626	401	257	101	64	26	2.04046
A3	212,005	52,891	33,595	20,490	8250	758	520	294	132	77	25	2.05311
A4	189,687	47,321	29,757	18,226	7414	625	400	256	100	64	25	2.04407
A5	194,525	48,229	30,592	18,491	7545	630	400	256	100	64	25	2.04986
A6	206,147	51,031	32,825	19,948	8050	798	479	279	103	77	25	2.05455
A7	190,423	47,626	29,980	18,298	7269	650	408	257	101	64	26	2.04154
A8	192,827	47,488	30,587	18,412	7642	724	400	256	100	64	25	2.04706
A9	191,726	47,389	30,321	18,297	7487	625	400	256	100	64	25	2.04627
A10	181,605	46,065	27,942	16,828	7184	639	402	256	100	64	25	2.03079
A11	214,385	53,198	33,776	20,587	8279	743	508	321	101	91	26	2.05413
A12	196,523	48,373	30,889	18,470	7441	692	402	256	100	64	25	2.05

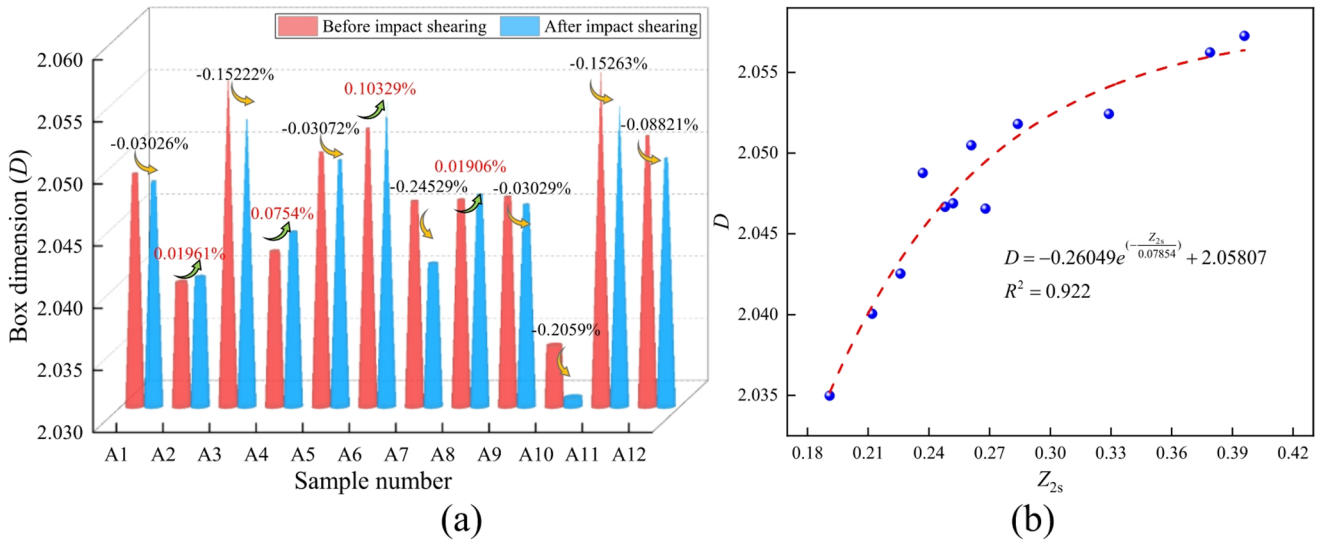

Fig. 10 Statistics of box counting dimensions. **a** Changes in D after impact shearing; **b** Relationship between D and Z_{2s}

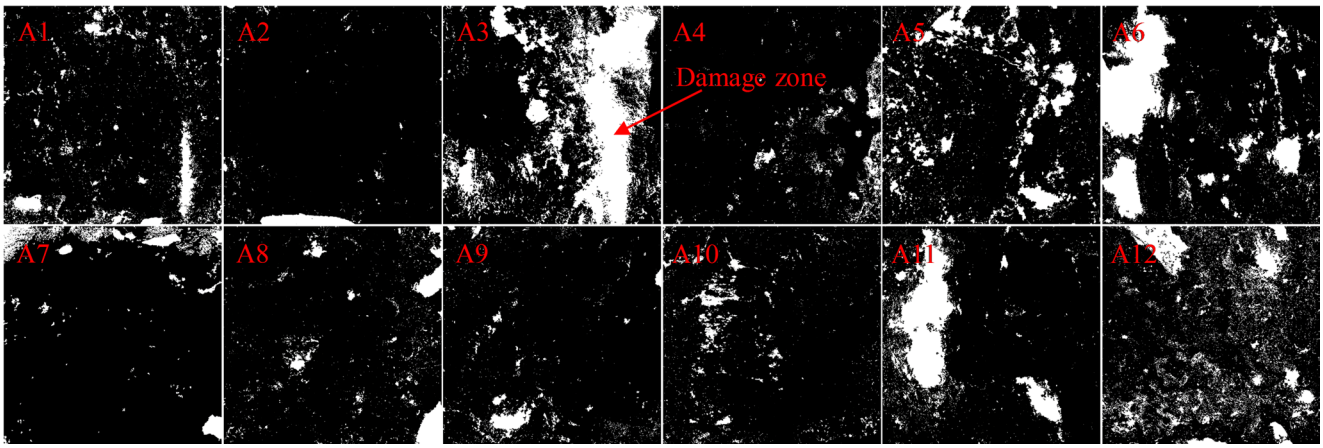

Fig. 11 Binary images of the fracture surfaces after experiments

the distribution of fracture damage zones, the box-counting dimension of the damage zones was calculated using the Box Count function in Fiji software.

Unlike the 3D fractal dimension of fracture surfaces, the 2D fractal dimension (H) of damage zone ranges from 1 to 2, with larger values indicating more complex damage zone morphologies. H values for the 12 fracture surfaces were summarized in Table 3. Shear damage zones of all samples exhibited fractal characteristics, with R^2 values reaching 0.99. The box-counting dimensions of the damage zones for 12 samples ranged from 1.241 to 1.742, with the three largest H values were observed in samples A3, A6, and A11. To explore the relationship between the H value of the damage zones and the fracture surface roughness, Fig. 12 illustrates how the H value varies with changes in Z_{2s} and $\theta_{max}/(C+1)$. Results showed that Z_{2s} and H had an exponential positive correlation, while the log ($\theta_{max}/(C+1)$) and log (H) exhibited a linear positive correlation.

3.3 Fracture space variation characteristics

The preceding sections investigated changes in the characteristics of the fracture surface after impact shearing under a confining pressure of 1 MPa. When confining pressure was increased to 5 MPa, the split-re-closed shale samples exhibited distinct damage characteristics. After impact shearing, all group B samples were scanned using 3D-XRM, with data processed via Avizo software.

Figure 13 presented 3D reconstruction results of the fracture spaces for samples B1–B9. After impact shearing, fracture structures of samples B1–B6 showed a marked increase in complexity. Sample B1 developed a fracture network where newly formed fractures were distributed along the bedding planes and interconnected. The volume of the fracture network and the fracture surface area generated after impact shearing were 1118.31 mm³ and 5915.28 mm², respectively. Assuming that the fracture space volume equals the product

Table 3 Statistics of box counts for damaged areas of the fracture surfaces

No.	Box size (pixel)										H	R^2
	1	2	3	4	6	8	12	16	32	64		
A1	236,005	74,065	40,104	26,639	15,480	10,756	6563	4640	1964	678	1.361	0.99
A2	64,174	18,414	9404	5994	3436	2425	1530	1184	641	324	1.241	0.99
A3	972,457	264,861	127,422	76,669	38,130	23,406	11,867	7348	2243	638	1.742	0.99
A4	136,672	51,492	30,747	21,406	12,839	8944	5284	3656	1460	559	1.306	0.99
A5	374,866	110,533	57,014	36,650	20,429	13,867	8233	5754	2262	703	1.458	0.99
A6	631,774	172,957	83,889	50,984	25,984	16,365	8761	5695	1978	636	1.636	0.99
A7	309,476	90,428	45,574	28,331	14,656	9365	5097	3440	1445	575	1.506	0.99
A8	173,079	53,384	28,827	19,168	11,585	8326	5363	3977	1808	665	1.279	0.99
A9	109,509	36,216	20,481	14,175	8772	6404	4159	3119	1423	524	1.227	0.99
A10	123,680	41,451	23,451	16,188	10,095	7368	4930	3704	1731	625	1.210	0.99
A11	454,526	128,703	64,124	39,837	20,899	13,324	7197	4656	1621	556	1.594	0.99
A12	487,099	170,719	98,555	67,519	39,365	26,519	14,716	9398	2973	729	1.525	0.99

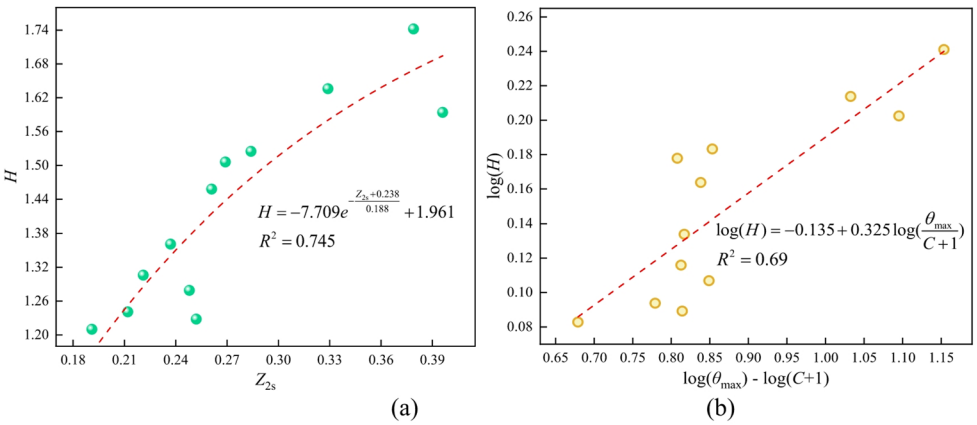

Fig. 12 Relationships between fracture surface roughness and fractal dimension of the damage zone. **a** Relationship between Z_{2s} and H; **b** Relationship between $\theta_{max}/(C+1)$ and H

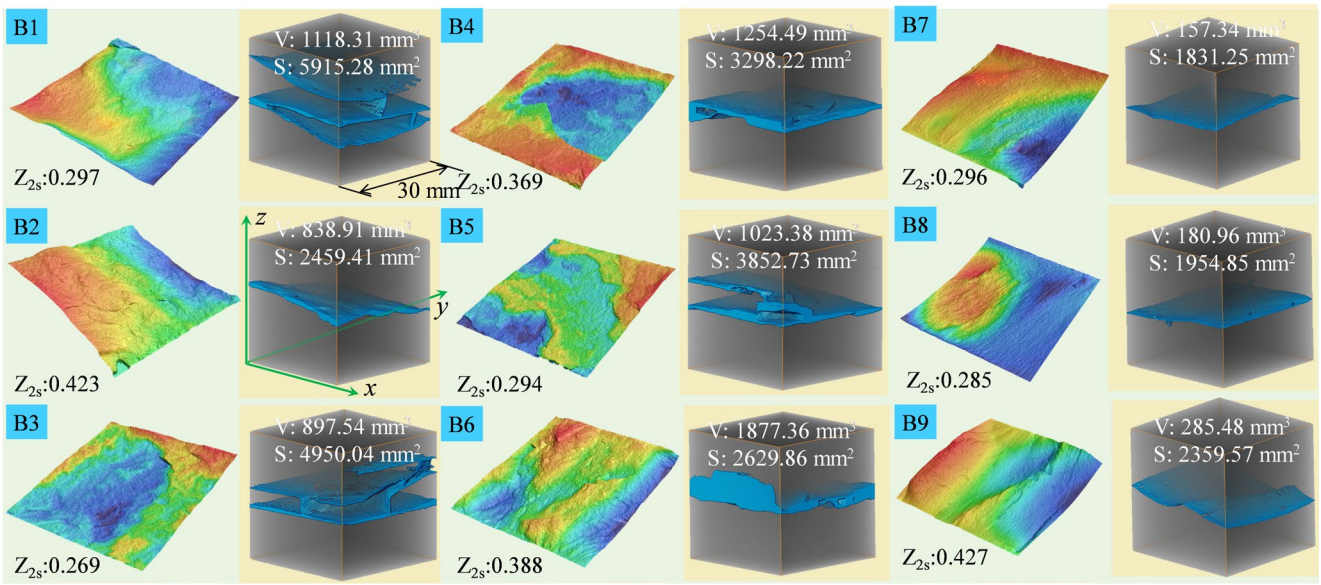

Fig. 13 Fracture spatial morphology of samples B1–B9

of the fracture surface area and fracture aperture, the ratio of fracture space volume to fracture surface area provides an approximate of the average fracture aperture. The fracture surface area was defined as half the surface area calculated by Avizo. Calculation results showed the average fracture apertures of samples B1–B6 were 0.378, 0.682, 0.363, 0.761, 0.531, and 1.428 mm, respectively. Samples B7–B10 (control group) were not subjected to impact shearing test, and their fracture surfaces were significantly smoother than those of the tested samples. Similar calculations yielded the average fracture apertures for samples B7–B10 were 0.172, 0.185, 0.242, and 0.123 mm, which clearly indicated that the average fracture aperture increased significantly after impact shearing.

Further investigation was performed to examine how fracture area and volume vary with Z_{2s}, as illustrated in Fig. 14. For non-impacted samples, both fracture volume and surface area exhibited a linear positive correlation with Z_{2s}. However, for samples B1–B6, fracture surface roughness showed no strict correlation with fracture volume or surface area. Owing to the pre-existing split fracture, stress wave propagation was complex, resulting in varied damage characteristics across samples. However, the general trends were observable from the figure: as Z_{2s} increases, the fracture volume increases and the surface area decreases. Consequently, the average fracture aperture increases with the increase of Z_{2s}.

3.4 Characteristics of shear slip and damage evolution

With an X-ray scanning resolution of 50 μm, the reconstructed space contained 600 slices in each direction. Taking samples B1 and B2 as examples, Fig. 15 shows the 2D

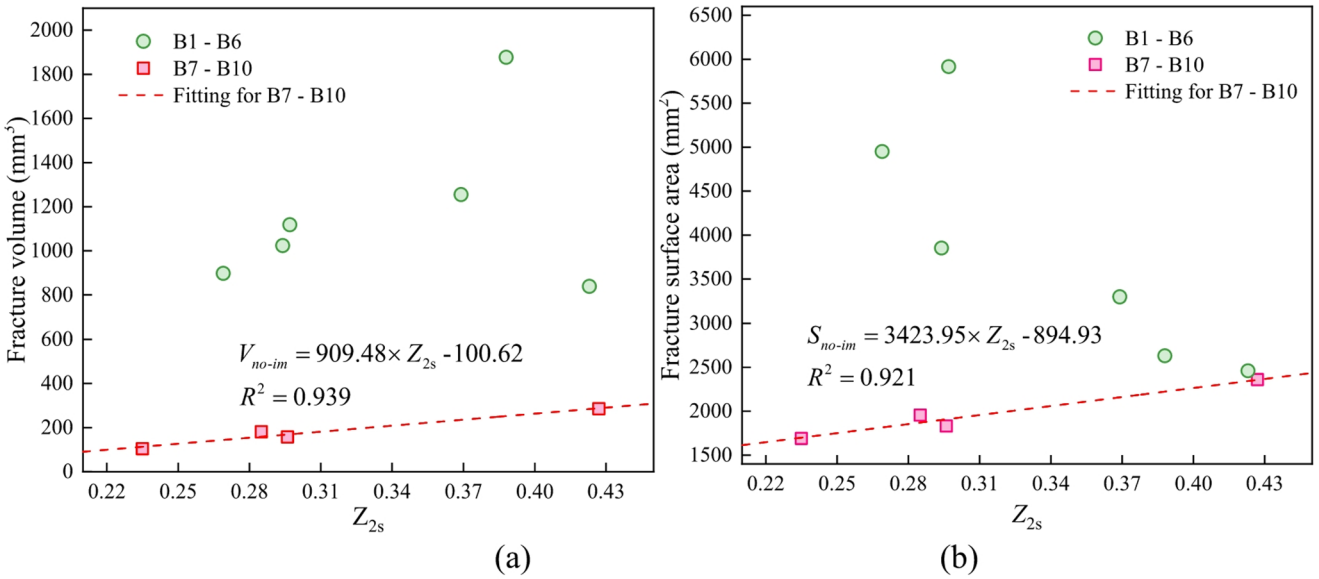

Fig. 14 Changes in fracture volume and sureface area with the variation of Z_{2s}. **a** Relation between volume and Z_{2s}; **b** Relation between surface area and Z_{2s}

slices of the fracture spaces in different directions. In these images, the blue arrows represent the shear direction of the fracture surface (along positive y-direction), and the numbers correspond to slice numbers. From the slices in the xz-plane, it can be seen that the fracture network in sample B1 is aligned with the bedding direction. In slices 234, 300, and 395, spalled rock debris is visible within the fractures; these debris particles can help support the fractures under closure stress. From the slices in the yz-plane, significant shear displacement occurred between the upper and lower segments of the split-re-closed sample. Due to fracture surface roughness, such shear displacement can also help prevent the fracture from closing under closing stress. In slice 353, spalled rock debris accumulated within the fracture during impact shearing, while the damage process of rock debris is visible in slice 599. Under impact loading, a thin rock fragment was formed along the bedding direction, subsequently moving along the shear direction under shear displacement. Finally, the fragment formed debris ①, followed by debris ②, and debris ③. Sample B2 had a different bedding direction from B1 but presented similar damage patterns. Results indicate that under impact shearing, the rock mass surrounding the pre-split surface was damaged, and bedding planes influenced the spatial structure of the fracture network due to their low strength. Additionally, after impact shearing, rock debris support structures and shear displacement support structures can form within fractures, preventing the fracture from closing.

A quantitative investigation of fracture space distribution was conducted by statistically analyzing the 2D fracture area of 600 slices along the impact direction (xz-plane), as shown in Fig. 16. As observed in Fig. 16a, fracture area distributions in slices of samples B7–B10 exhibited relatively uniform characteristics: sample B7 showed fracture areas ranging from 4 to 6 mm²; samples B8 and B10 exhibited fracture areas concentrated between 2 and 4 mm²; and most slices of sample B9 maintained fracture areas between 6 and 8 mm². Figure 16b presented fracture area distribution of samples B1–B4 after impact shearing. It is evident that post-impact fracture area underwent significant changes, characterized by notable fluctuations and uneven distribution due to the shear displacement of the fracture surface and the spalling of rock debris. For sample B1, fracture areas in slices 0–500 ranged from 30 to 40 mm², 5–10 times larger than those of non-impacted samples. In slices 500–600, the fracture area further increased from 35 to 50 mm². Sample B2 exhibited fracture area variation of 15–35 mm² with a periodic "increase-decrease" pattern, which was attributed to impact-induced shear displacement causing alternating "contact-separation" spatial distribution between upper and lower rock blocks. Samples B3 and B4 also showed distinct uneven distribution characteristics after impact. Results indicate that the fracture space distribution is uniform in non-impact samples, while post-impact shearing significantly increased fracture space by approximately one order of magnitude. Fracture areas in the slices exhibited

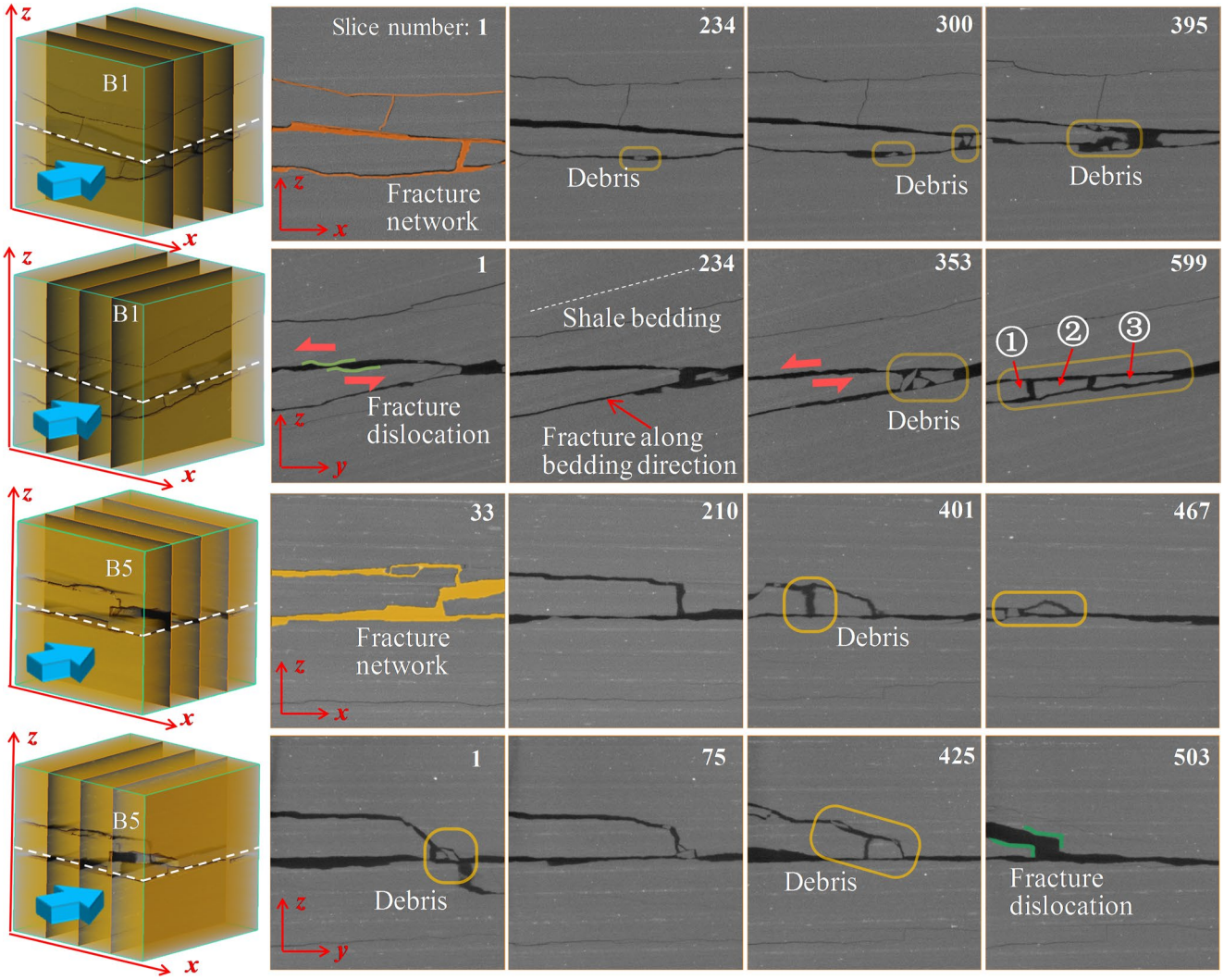

Fig. 15 Slices of fractures in different directions

fluctuating variations, with troughs representing contact areas between upper and lower rock masses. Even at trough positions, fracture areas remained over three times larger than those of non-impacted fractures, reflecting the complex fracture network formed by impact and the substantial expansion of fracture space.

Figure 17 presented the fracture area of 600 slices for each sample. From Fig. 17a, for sample B7, the 25th and 75th percentiles were 5.12 mm² and 5.43 mm², respectively, with a box length of only 0.31 mm². The small box length indicates uniform fracture area distribution, confirming that the split-re-closed sample underwent no significant shear displacement. The complex-shaped fracture space in each slice was simplified to a rectangular geometry. Based on the median value of 5.27 mm², calculations yielded an average fracture aperture of approximately 0.176 mm. Similarly, average fracture apertures for samples B8–B10 were 0.12, 0.244, and 0.119 mm, respectively, which are generally consistent with the results in Sect. 3.3. From Fig. 17b, it is evident that post-impact shearing not only increased fracture area but also increased the degree of dispersion in the samples. Average fracture apertures for samples B1–B4 were 1.232, 0.993, 0.931, and 1.33 mm, respectively. Comparative analysis shows that the average fracture aperture increased by 5 to 19 times after impact shearing.

4 Discussions

Due to limitations of the SHPB impact-shearing tests, the damage process is difficult to visualize and characterize—a challenge that can be resolved using numerical simulation. A 2D numerical model corresponding to this study was established based on the coupling method of FLAC and

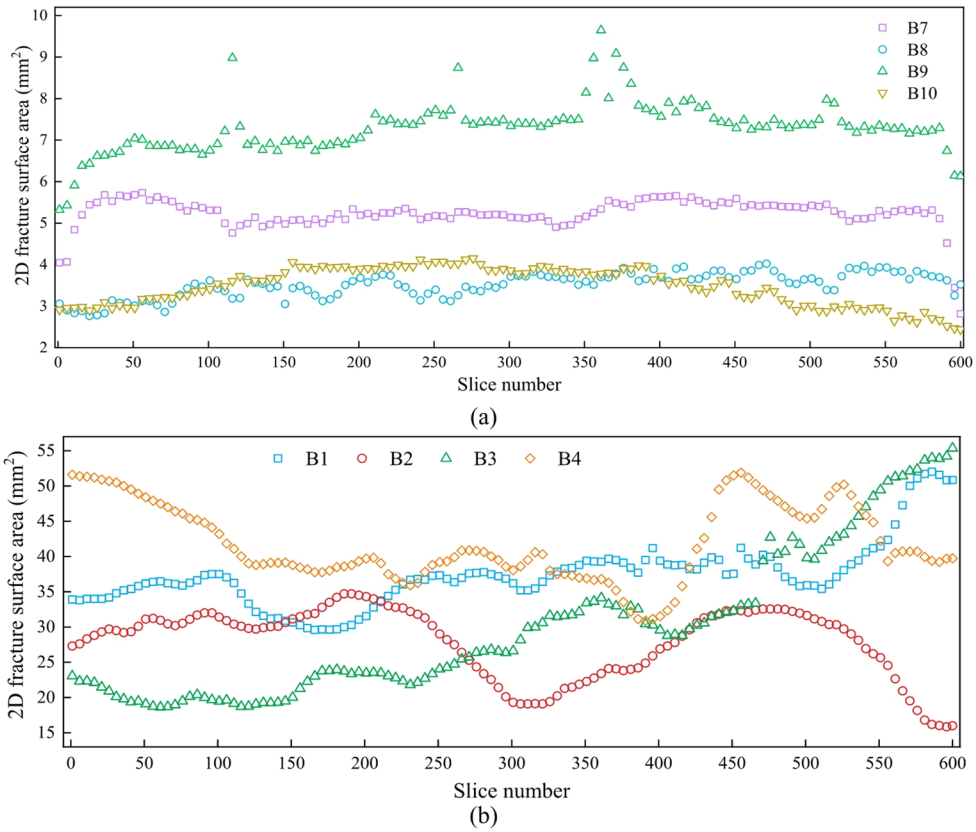

Fig. 16 Fracture surface areas of 2D slices. **a** Samples B7–B10; **b** Samples B1–B4

PFC (Tang et al. 2022a, b). The joint profile in the model was derived from the cross-section of the sample A12. Figure 18 showed the established model, with model parameters listed in Table 4.

Figure 19a showed the numerical simulation results of the fracture damage process under 1 MPa confining pressure. Line thickness in the figure denotes the magnitude of contact forces, with thicker lines indicating greater force; line orientation indicated contact locations and directions. At $t=0$ ms, the rock model was in a stable equilibrium state. A local magnification revealed that contact points (shown by light blue lines) between the two rock blocks exhibited diverse orientations. At $t=0.02$ ms, the stress wave reached the upper rock block. Contact force distribution showed that contact forces between the two rock blocks exhibited similar angular distributions. Magnified views revealed stress concentration-induced damage initiation. At $t=0.05$ ms, only one contact point remained due to the shear-dilatation effect, with other contact points disappearing. Stress continued to increase, leading to damage propagation along the bedding plane. At $t=0.1$ ms, fracturing occurred at the contact point, followed by re-contact between the upper and lower rock blocks. Results indicate that under impact shearing, regions with higher local fracture surface roughness are the first to undergo damage, resulting in non-uniform

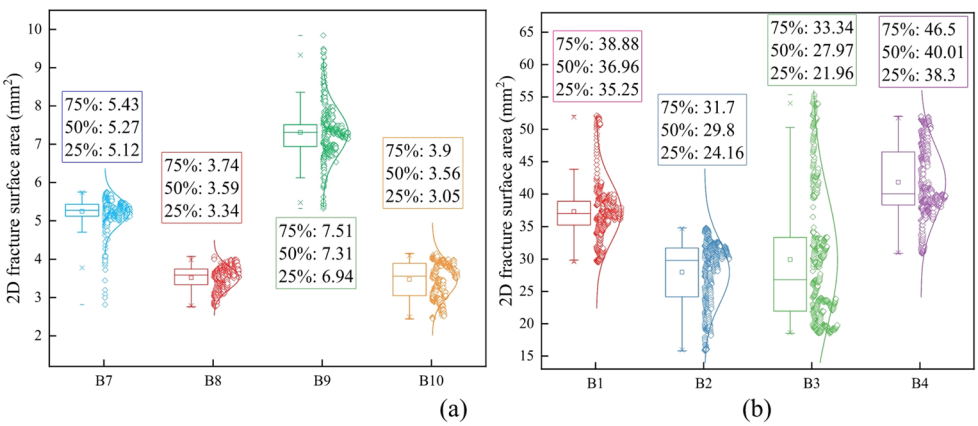

Fig. 17 Statistics of fracture areas. **a** Samples B7–B10; **b** Samples B1–B4

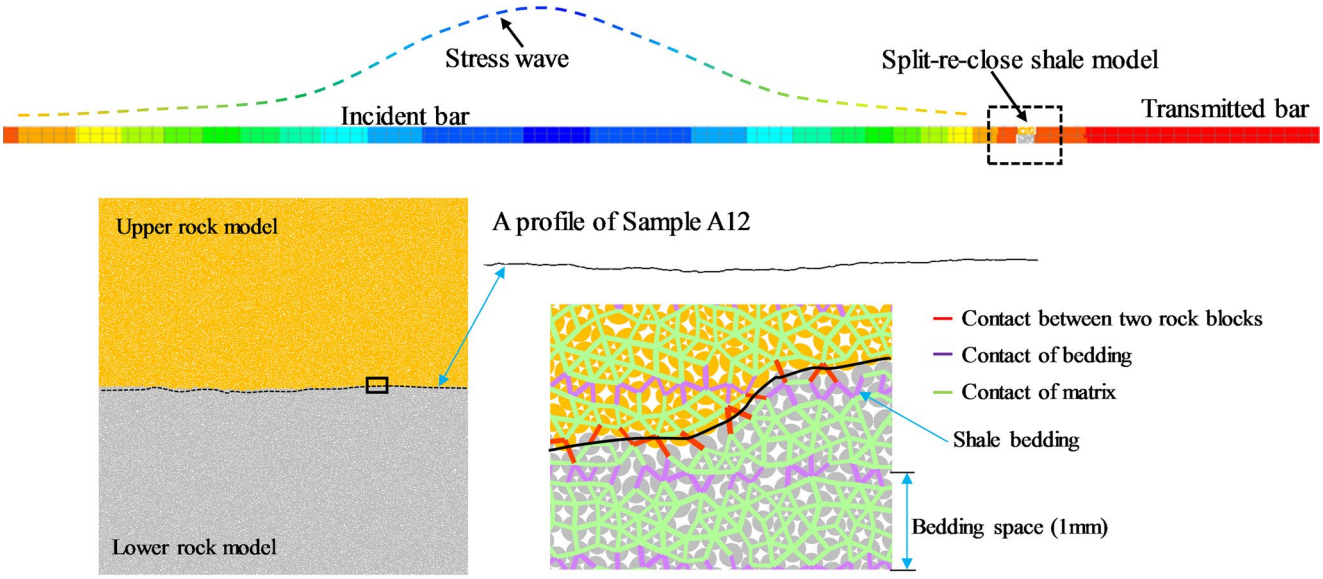

Fig. 18 Numerical model for modified SHPB and split-re-closed sample

Table 4 Model parameter setting

Shale matrix		Shale bedding	
Contact model	Flatjoint	Contact model	Linearpbond
emod, GPa	17.3	emod, GPa	17.3
kratio	2.8	kratio	2.3
fj_nr	2	Emod (bond), GPa	17.3
fj_ten, MPa	35.2	kratio (bond)	2.3
fj_coh, MPa	78.5	pb_ten, MPa	25.1
fj_fa, °	38	pb_coh, MPa	30.5
		pb_fa, °	10

damage distribution along the fracture surface, consistent with observations in Fig. 6.

Figure 19b showed fracture surface damage variations for samples A6 and A11 before and after impact shearing. The two peaks on their fracture surfaces were damaged after impact, while the region between these two damaged areas remained nearly intact. Post-impact fracture surface damage was mainly characterized by the spalling of rock debris at areas of higher local roughness, which corresponded to the numerical simulation results.

Figure 20 presented the numerical results of the split-re-closed shale model under a confining pressure of 5 MPa. A shale model with a bedding angle of −10° has similar bedding structure to that of sample B1; the shale model with horizontal bedding is similar to sample B4. Figure 20 showed that the bedding direction has a significant influence on fracture propagation. At a bedding angle of −10°, damage generated in the rock mass on both sides of the re-closed fracture surface propagated along the bedding direction. Combined damage to the shale matrix and bedding structure resulted in layered failure. For the model with horizontal bedding, damage was also concentrated on the bedding plane, with numerical results showing good agreement with experimental observations. Orange particles in the figure represent small-sized rock debris formed under the impact shearing. Models with a bedding angle of −10° or 0° generated relatively few small-sized debris, whereas a large quantity of small-sized debris was produced in the model with a 10° bedding angle. Increased debris accumulation within fractures may enhance the fracture support capacity under closure stress.

5 Conclusions

In this paper, the damage characteristics of split-re-closed shale samples were studied through the SHPB impact-shearing system. We explored the impact shearing damage characteristics of fracture surfaces at a lower confining pressure by means of fracture surface roughness characterization methods, and analyzed the variation characteristics of the fracture space of shale samples under a higher confining pressure using X-ray tomography. Finally, through numerical simulation methods, a simple discussion was carried out on the shale impact shearing damage process and the influence of bedding structures on crack propagation from a microscopic perspective. The following are the main conclusions of this study.

(1) Under a lower confining pressure, impact shearing induces non-uniform damage on fracture surfaces, with regions of higher local roughness being preferentially damaged. Characterized by parameters such as Z_{2s} and

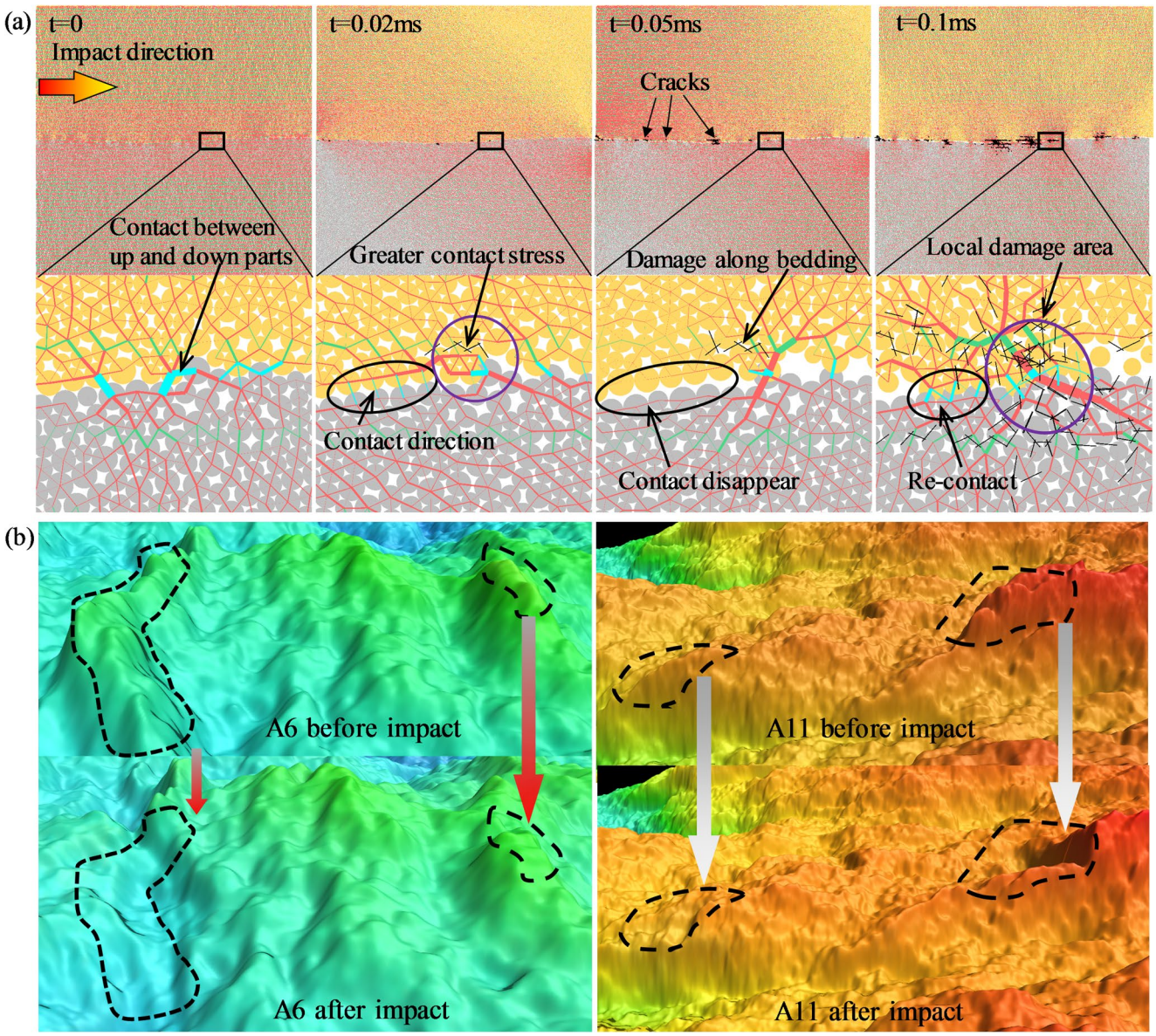

Fig. 19 **a** Damage process of numerical model, **b** Fracture surface damage of samples A6 and A11

$\theta_{max}/(C+1)$, fractal dimensions (D and H), fracture surface roughness generally decreases after impact, though local increases in specific subregions are observed. Z_{2s} and $\theta_{max}/(C+1)$ of the fracture surface exhibit a linear positive correlation; D and Z_{2s} show an exponential positive correlation. The H values of damaged areas of the fracture surfaces after impact shearing show exponential correlations with both Z_{2s} and $\theta_{max}/(C+1)$. The surface damage primarily manifests as debris spalling in elevated roughness areas.

(2) Under a higher confining pressure, impact shearing significantly enhances fracture space complexity. Post-impact samples develop interconnected fracture networks along bedding planes, with average fracture apertures increasing by 5 to 19 times compared to non-impacted controls. Shear displacement and debris accumulation form supportive structures within fractures, preventing fracture closure under confining stress. Quantitative analysis of X-ray tomography data confirms uneven distribution of fracture areas in slices, reflecting substantial expansion of fracture space. Different bedding angles affect the damage evolution and final spatial structure of the fracture space.

(3) Numerical simulations using FLAC-PFC coupling validate the experimental damage evolution process: stress concentration initiates damage at high-roughness contact points, followed by propagation along bedding planes. Bedding orientation significantly influences

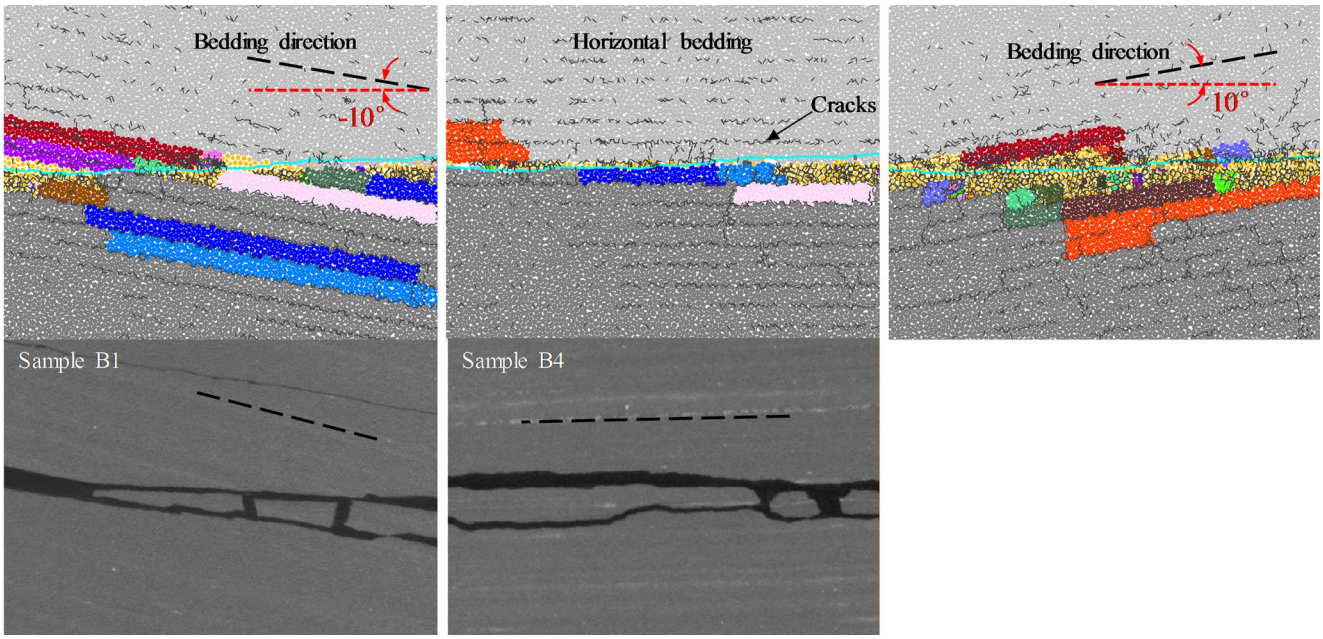

Fig. 20 Numerical and experimental results of shale damge under 5 MP confining pressure

fracture propagation patterns— models with different bedding angles exhibit varied damage modes and debris production. Increased debris generation at a 10° bedding angle enhances fracture support capacity, aligning with experimental findings on debris-indeced fracture stability.

Acknowledgements This work was financially supported by the National Key R&D Program of China (2020YFA0711800), and China Postdoctoral Science Foundation (2025M771795).

Author contributions Wei Tang: Conceptualization, Methodology, Software, Data curation. Cheng Zhai: Project administration, Funding acquistion. Ting Liu: Investigation, Formal analysis. Jizhao Xu: Supervision & Investigation. Yong Sun: Formal analysis. Yangfeng Zheng: Formal analysis. Yuzhou Cong: Writing – original draft. Yu Wang: Writing – original draft. Chengjian Pi: Writing – review & editing.

Declarations

Competing interests The authors declare that they have no known competing financial interests or personal relationships that could have appeared to influence the work reported in this paper.

References

Asala HI, Ahmadi M, Taleghani AD (2016) Why re-fracturing works and under what conditions. SPE Annual Tech Conf Exhib. https://doi.org/10.2118/181516-MS

Barton N (1973) Review of a new shear-strength criterion for rock joints. Eng Geol 7:287–332

Chen J, Li X, Cao H et al (2022) Experimental study on the mechanism of coupled dynamic–static fracturing on damage evolution and crack propagation in tight shale. Energy Rep 8:7037–7062

Fan X, Luo N, Liang H et al (2021) Dynamic breakage characteristics of shale with different bedding angles under the different ambient temperatures. Rock Mech Rock Eng 54:3245–3261

Feng X, Gong B, Liang Z et al (2023) Study of the dynamic failure characteristics of anisotropic shales under impact Brazilian splitting. Rock Mech Rock Eng 57:2213–2230

French S, Rodgerson JL, Feik CJ (2014) Re-fracturing horizontal shale wells: case history of a Woodford shale pilot project. SPE Hydraulic Fracturing Technol Conf Exhib. https://doi.org/10.2118/168607-MS

Grasselli G, Egger P (2003) Constitutive law for the shear strength of rock joints based on three-dimensional surface parameters. Int J Rock Mech Min Sci 40:25–40

Gu Y, Gao D, Diao B et al (2022) Optimization design method of infill well trajectory with bypassing obstacles in the fractured area of shale gas reservoir. J Pet Sci Eng 208:109779

Guo K, Zhang B, Aleklett K et al (2016a) Production patterns of eagle Ford shale gas: decline curve analysis using 1084 wells. Sustainability 8:973

Guo K, Zhang B, Höök M et al (2016b) Production decline laws for shale gas wells in Haynesville, US. Petroleum Sci Bull 02:293–305. https://doi.org/10.3969/j.issn.2096-1693.2016.02.025

Huan J, He M, Zhang Z et al (2024) Reverse calculation and quantitative estimation of JRC3D for rough rock fracture surfaces in various shear directions. Physics and Chemistry of the Earth, Parts A/B/C 134:103587

Kong L, Ostadhassan M, Tamimi N et al (2019) Refracturing: well selection, treatment design, and lessons learned—a review. Arab J Geosci 12:1–13

Lei Q, Weng D, Luo J et al (2019) Achievements and future work of oil and gas production engineering of CNPC. Pet Explor Develop 46:145–152

Liu J, Li Y, Zhang H (2015) Study on shale's dynamic damage constitutive model based on statistical distribution. Shock Vib 2015:1–8

Liu H, Feng X, Liu L et al (2023) Mechanical properties and failure characteristics of anisotropic shale with circular hole under combined dynamic and static loading. Int J Rock Mech Min Sci 170:105524

Luo N, Fan X, Cao X et al (2022) Dynamic mechanical properties and constitutive model of shale with different bedding under triaxial impact test. J Pet Sci Eng 216:110758

Lv H, Cheng Z, Xie F et al (2024) Study on hydraulic fracturing prevention and control of rock burst in roof of deep extra-thick coal seam roadway group. Sci Rep 14:29537

Magsipoc E, Zhao Q, Grasselli G (2020) 2D and 3D roughness characterization. Rock Mech Rock Eng 53:1495–1519

Movassagh A, Haghighi M, Zhang X et al (2021) A fractal approach for surface roughness analysis of laboratory hydraulic fracture. J Nat Gas Sci Eng 85:103703

Patzek TW, Male F, Marder M (2013) Gas production in the Barnett Shale obeys a simple scaling theory. Proc Natl Acad Sci U S A 110:19731–19736

Saputra W, Kirati W, Patzek TW (2021) Generalized extreme value statistics, physical scaling and forecasts of gas production in the Haynesville shale. J Nat Gas Sci Eng 94:104041

Schindelin J, Arganda-Carreras I, Frise E et al (2012) Fiji: an open-source platform for biological-image analysis. Nat Methods 9:676–682

Shi X, Yao W, Liu D et al (2019) Experimental study of the dynamic fracture toughness of anisotropic black shale using notched semi-circular bend specimens. Eng Fract Mech 205:136–151

Shi W, Zhang C, Jiang S et al (2022) Study on pressure-boosting stimulation technology in shale gas horizontal wells in the Fuling shale gas field. Energy 254:124364

Tang W, Zhai C, Xu J et al (2022a) Numerical simulation of expansion process of soundless cracking demolition agents by coupling finite difference and discrete element methods. Comput Geotech 146:104699

Tang W, Zhai C, Yu X et al (2022b) Dynamic Brazilian splitting experiment of bedding shale based on continuum-discrete coupled method. Int J Impact Eng 168:104289

Vincent M (2010) Refracs: why do they work, and why do they fail in 100 published field studies? SPE Annual Technical Conference and Exhibition Florence Italy September 2010. https://doi.org/10.2118/134330-MS

Vincent M (2011) Restimulation of unconventional reservoirs: when are refracs beneficial? J Can Pet Technol 50:36–52

Vogler D, Walsh SDC, Bayer P et al (2017) Comparison of surface properties in natural and artificially generated fractures in a crystalline rock. Rock Mech Rock Eng 50:2891–2909

Wang T, Chen M, Wu J et al (2021) Making complex fractures by refracturing with different plugging types in large stress difference reservoirs. J Pet Sci Eng 201:108413

Wang X, Zhu Z, Zhou L et al (2022) Study on the effects of joints orientation and strength on failure behavior in shale specimen under impact loads. Int J Impact Eng 163:104162

Xie Q, Li S-x, Liu X-l et al (2020) Effect of loading rate on fracture behaviors of shale under mode I loading. J Cent South Univ 27:3118–3132

Yang G, Li X, Bi J et al (2019) Dynamic crack initiation toughness of shale under impact loading. Energies 12:1636

Yang G, Liu J, Li X et al (2020) Effect of temperature on shale strength under dynamic impact loading. Arab J Geosci 13:1–9

Yang BG, Xie J, Yang YM et al (2024) Anisotropy and size effect of the fractal characteristics of rock fracture surfaces under microwave irradiation: an experimental research. Fractals 32:2340123

Yi Y, Wang L, Li J et al (2022) Optimization of re-fracturing method and fracture parameters for horizontal well in Mahu conglomerate oil reservoir. Front Energy Res 10:856524